

## Photo-Fenton-Based Degradation of Methylene Blue Dye Using Hydroxyapatite Nanoparticles Doped with Fe<sub>3</sub>O<sub>4</sub>/γ-Fe<sub>2</sub>O<sub>3</sub>

Fausto E. Bimbi Junior,<sup>a</sup> Camila G. Neves,<sup>a</sup> Maria D. L. do Nascimento,<sup>a</sup>  
Evaristo A. Falcão<sup>✉</sup><sup>a</sup> and Willyam R. P. Barros<sup>✉</sup><sup>\*,a</sup>

<sup>a</sup>Grupo de Eletrocatalise e Tecnologia Eletroquímica, Faculdade de Ciências Exatas e Tecnologia,  
Universidade Federal da Grande Dourados, Rodovia Dourados/Itahum, km 12,  
Unidade II, 79804-970 Dourados-MS, Brazil

In this study, we evaluated the catalytic properties of hydroxyapatite (HA) nanoparticles (NPs) doped with Fe<sub>3</sub>O<sub>4</sub>/γ-Fe<sub>2</sub>O<sub>3</sub> for the degradation of methylene blue (MB) dye using a photo-Fenton process at pH 2.5, 7.0, and 9.0. The HA NPs were characterized using X-ray diffraction, scanning electron microscopy, Fourier-transform infrared spectrometry, Raman spectroscopy, thermogravimetric analysis, fluorescence spectrometry, and point of zero charge experiments. Upon using unmodified HA NPs, 1.33 mL of H<sub>2</sub>O<sub>2</sub> 30% (v/v), and ultraviolet radiation (125 W Hg lamp), the discoloration values achieved at pH 2.5, 7.0, and 9.0 were 88.4, 44.8, and 58.1%, respectively. For the HA NPs modified with Fe<sub>3</sub>O<sub>4</sub>/γ-Fe<sub>2</sub>O<sub>3</sub>, the composition Ca<sub>2.5</sub>Fe<sup>II</sup><sub>2.5</sub>Fe<sup>III</sup><sub>5</sub>(PO<sub>4</sub>)<sub>6</sub>(OH)<sub>2</sub> yielded the best results during the photo-Fenton-based process, and discolorations of 100, 100, and 95.2% were achieved at pH 2.5, 7.0, and 9.0, respectively. To confirm the effectiveness of the Ca<sub>2.5</sub>Fe<sup>II</sup><sub>2.5</sub>Fe<sup>III</sup><sub>5</sub>(PO<sub>4</sub>)<sub>6</sub>(OH)<sub>2</sub> NPs, the total organic carbon (TOC) and toxicity effects on *Lactuca sativa* L. were evaluated, and reproducibility tests were performed. The TOC removal of the Ca<sub>2.5</sub>Fe<sup>II</sup><sub>2.5</sub>Fe<sup>III</sup><sub>5</sub>(PO<sub>4</sub>)<sub>6</sub>(OH)<sub>2</sub> NPs was ca. 90% and the toxicity of the MB dye was eliminated after 120 min of reaction; moreover, the NPs retained their physical stability and activity and were reused for 11 consecutive degradation experiments.

**Keywords:** magnetite, maghemite, heterogeneous Fenton process, structural modification

### Introduction

Advanced oxidation processes used as alternative wastewater treatment methods require large amounts of energy and/or chemicals to produce reactive oxidizing species, most commonly hydroxyl radicals (•OH), which are highly reactive, non-selective radicals that can completely or partially oxidize numerous organic species.<sup>1-4</sup>

In addition to titanium oxide, iron-oxide-based nanomaterials, such as magnetite (Fe<sub>3</sub>O<sub>4</sub>), hematite (α-Fe<sub>2</sub>O<sub>3</sub>), and maghemite (γ-Fe<sub>2</sub>O<sub>3</sub>), have been extensively studied, and are model nanoparticles (NPs) owing to their remarkable catalytic and photocatalytic performances.<sup>5-8</sup>

To enhance the catalytic effect of these nanomaterials, support materials have been developed by adding acid/base sites and increasing selectivity, thereby facilitating the interactions between various media and NPs. Several types of support materials, such as coke and alumina, and

a promising catalytic support, namely hydroxyapatite (HA; Ca<sub>10</sub>(PO<sub>4</sub>)<sub>6</sub>(OH)<sub>2</sub>) have been commonly used by researchers.<sup>9,10</sup> HA NPs can be used as heterogeneous nanomaterials and exhibit remarkable photocatalytic properties for the degradation of emerging pollutants.<sup>11-13</sup>

The structure of HA NPs, which are calcium phosphates, depends on the stoichiometric Ca/P ratio, which typically ranges between 0.5 and 2.0. Changes in the Ca/P ratio cause changes in the properties of HA NPs. The HA NPs with a Ca/P ratio of 1.67 are the most stable and least soluble among all HA NPs; moreover, they present the highest energy response to photocatalysis.<sup>14,15</sup>

Several synthesis methods have been used to fabricate HA NPs, and two specific types of nanomaterials can be obtained by adjusting the synthesis temperature, as follows. The HA NPs fabricated at high temperatures present good crystallinity and large crystals, whereas those synthesized at low temperatures exhibit poor crystallinity and small crystals.<sup>16-18</sup>

The structure of HA NPs favors the partial replacement of the ions in their structure, and isomorphous substitution

\*e-mail: willyambarros@ufgd.edu.br

Editor handled this article: Jaísa Fernandes Soares

occurs easily.<sup>19</sup> Metal cations such as lead (Pb<sup>2+</sup>), cadmium (Cd<sup>2+</sup>), copper (Cu<sup>2+</sup>), zinc (Zn<sup>2+</sup>), strontium (Sr<sup>2+</sup>), cobalt (Co<sup>2+</sup>), iron (Fe<sup>2+</sup>), can replace the Ca<sup>2+</sup> cations in the structure of HA. Conversely, the phosphate (PO<sub>4</sub><sup>3-</sup>) and hydroxyl (OH<sup>-</sup>) groups of HA can be replaced by carbonate (CO<sub>3</sub><sup>2-</sup>) and fluorine (F<sup>-</sup>) or/and chlorine (Cl<sup>-</sup>) anions, respectively. However, the ionic radii of the substituent ions are different from those of the parent ions; moreover, their ionic interactions are different. These substitutions can alter the crystallographic structure, crystal dimensions, shape, stability, and solubility of HA NPs.<sup>20</sup>

In this sense, the modification of the HA crystallographic structure with iron-oxide-based nanomaterials (e.g., Fe<sub>3</sub>O<sub>4</sub>/γ-Fe<sub>2</sub>O<sub>3</sub>) has captured the interest of scientists, since Fe ions can be used as Fenton catalysts and promote the formation of abundant •OH species owing to the reaction mechanisms.<sup>21,22</sup> The Fenton process is based on the reaction between H<sub>2</sub>O<sub>2</sub> and Fe<sup>2+</sup> or Fe<sup>3+</sup> ions and is used for the degradation of organic compounds. The efficiency of the Fenton process is ascribed to the ability of •OH species, which are powerful non-selective oxidants, to oxidize emerging pollutants and promote the removal of large amounts of highly recalcitrant compounds.<sup>23-25</sup> HA NPs modified with iron-oxide-based nanomaterials presented remarkable catalytic stability because they could be recycled several times without activity loss or changes in structure and properties.<sup>26,27</sup>

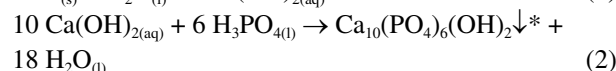
To impart the aforementioned properties to HA NPs, in this study, HA NPs were doped with Fe<sub>3</sub>O<sub>4</sub>/γ-Fe<sub>2</sub>O<sub>3</sub>, and the effect of the modifications on the photo-Fenton-based degradation of methylene blue (MB) dye (C.I. 52015) was investigated. Our results indicate that this method yielded good discoloration results, significantly decreased the total organic carbon (TOC) levels, shortened reaction times, and lowered byproduct toxicity.

## Experimental

### Synthesis of HA NPs

Unmodified HA NPs were synthesized using a coprecipitation method and calcium oxide (CaO, Sigma-Aldrich, São Paulo, Brazil), phosphoric acid (H<sub>3</sub>PO<sub>4</sub>, Sigma-Aldrich, São Paulo, Brazil), and ammonium hydroxide (NH<sub>4</sub>OH, Dinâmica, Indaiatuba, Brazil), as follows. CaO (2.78 g) was added to 200 mL of ultrapure water (Millipore Milli-Q 18.2 MΩ cm) (equation 1) under mechanical stirring for 20 min at ca. 25 °C. Subsequently, the temperature was increased to 80 °C. Thereafter, 1.5 mL of concentrated H<sub>3</sub>PO<sub>4</sub> (85 wt.%) was added dropwise to

the reaction mixture (equation 2), and concentrated NH<sub>4</sub>OH was used to maintain a pH > 8.0. A white precipitate started to form, and the solution was stirred for 40 min. Next, the mixture was filtered, washed several times with ultrapure water, and dried at 70 °C for 24 h.



\*HA NPs

To synthesize HA NPs doped with Fe<sup>2+</sup>/Fe<sup>3+</sup>, iron(II) chloride tetrahydrate (FeCl<sub>2</sub>·4H<sub>2</sub>O) and iron(III) chloride hexahydrate (FeCl<sub>3</sub>·6H<sub>2</sub>O) were used as precursors, and 1 mL of a 0.5 mol L<sup>-1</sup> sodium tetraborohydride (NaBH<sub>4</sub>, Dinâmica, Indaiatuba, Brazil) solution was used as the reducing agent used to prevent the total oxidation of Fe<sup>2+</sup> ions.

First, FeCl<sub>2</sub>·4H<sub>2</sub>O and FeCl<sub>3</sub>·6H<sub>2</sub>O were added to HA at ca. 25 °C. Next, 2 mL of a 0.5 mol L<sup>-1</sup> NaBH<sub>4</sub> solution and 100 mL of a 2 mol L<sup>-1</sup> sodium hydroxide (NaOH) solution were added to the reaction mixture, and a brown precipitate was formed. The solution was stirred until the temperature reached 80 °C, and then, the procedure followed the same steps used to fabricate the unmodified HA NPs. After, the reaction mixture was stirred for 40 min, the NPs were separated using a neodymium magnet, washed several times with ultrapure H<sub>2</sub>O, and dried at 70 °C for 24 h. All the chemicals were used without further purification. The HA NPs doped with Fe<sup>2+</sup>/Fe<sup>3+</sup> obtained by replacing a fraction of the Ca<sup>2+</sup> ions in the structure of HA with Fe<sup>2+</sup>/Fe<sup>3+</sup> ions (1:2 mol/mol) are denoted as HAF60, HAF70, HAF75, and HAF100, where the numbers represent the theoretical percentages of Ca<sup>2+</sup> ions substituted by Fe<sup>2+</sup>/Fe<sup>3+</sup> ions.

The compositions of the HAF60, HAF70, HAF75, and HAF100 NPs, which were determined using stoichiometric calculations and the corresponding amounts of precursors are summarized in Table S1 (Supplementary Information (SI) section).

### HA NPs characterization

The HA NPs were subjected to X-ray diffraction (XRD) analysis using a D8 Advance instrument (Bruker, Ettlingen, Baden-Württemberg, Germany) equipped with a Cu Kα radiation source (λ = 1.5406 Å) operated at 40 kV and 30 mA. The XRD patterns were obtained via continuous scanning in the 2θ range of 20-60°, at a step size of 0.01° after 60 s of scanning. The crystallite sizes (D) were calculated using the Debye-Scherrer equation (equation 3)

and the data for the crystallographic planes (211) and (311) of  $\text{Fe}_3\text{O}_4$ , which corresponded to the unmodified and modified HA NPs, respectively.<sup>28</sup>

$$D = \left( \frac{0.9\lambda}{\beta \cos\theta} \right) \quad (3)$$

where  $\beta$  is the full width at half maximum (FWHM).

The morphologies of the modified and unmodified NPs were examined using a VEGA3 (TESCAN, Brno, Czech Republic) scanning electron microscopy (SEM) operated at 10 kV.

The Fourier-transform infrared (FTIR) spectroscopy profiles of the modified and unmodified NPs were obtained using a 4100 spectrometer (Jasco, Tokyo, Japan) in the wavenumber range of 400–4000  $\text{cm}^{-1}$  at a resolution of 4  $\text{cm}^{-1}$ . The modified and unmodified NP powders were mixed with potassium bromide (KBr) and macerated in an agate mortar (sample:KBr = 1:99 (m/m)). A manual press was used to obtain thin compact samples, which were then attached to the spectroscope holder such that the laser was focused at the center of the sample.

Raman spectroscopy was performed using a tip-enhanced Raman scattering device (Horiba Jobin-Yvon, Palaiseau, France) with a resolution of 500 nm equipped with a confocal microscope coupled (“XYZ” automatic table) featuring a 488 nm laser with a spectral window range of 40–1000 nm.

Thermogravimetric (TG) analyses were performed using a STA449 F3 Jupiter<sup>®</sup> thermogravimetric analyzer (Netzsch, Selb, Germany). For the TG experiments, ca. 5.0 mg sample was added to an  $\alpha$ -alumina crucible, followed by purging with air at a flow rate of 50  $\text{mL min}^{-1}$ ; the temperature was increased to 1,000  $^{\circ}\text{C}$  at a heating rate of 10  $^{\circ}\text{C min}^{-1}$ .

Fluorescence measurements were performed in the wavelength range of 400–900 nm using a portable spectrofluorometer (Dunedin, Florida, USA) comprising a diode laser operated at 405 nm, a monochromator (USB 2000 F L, Ocean Optics), a fiber-type “Y,” and a computer.

The point of zero charge ( $\text{pH}_{\text{PZC}}$ ) is the pH at which the charge at the surface of an adsorbent material is zero in respect to the  $\text{H}^+$  and  $\text{OH}^-$  ions in the media.<sup>29</sup> Eleven measurements points were used for these experiments. In brief, 0.1 g of each type of HA NPs and 100 mL of a NaCl solution 1% (m/v) were added to a 250 mL Erlenmeyer flask, and then the pH was measured using a 0.1 mol  $\text{L}^{-1}$  NaOH or a 0.1 mol  $\text{L}^{-1}$  HCl solution. Next, the solutions were stirred at 120 rpm and 25  $^{\circ}\text{C}$  using a shaking table, and the pH was measured again after 24 h.

## MB dye degradation

The degradation experiments were performed in a single-compartment Pyrex glass reactor equipped with a mechanical stirrer and placed in a wooden box to eliminate external interferences and using MB dye (Sigma-Aldrich, São Paulo, Brazil) as the target molecule. In brief, 100 mL of a 100  $\text{mg L}^{-1}$  MB dye solution was added to acidic, neutral, or alkaline media (pH 2.5, 7.0, or 9.0, respectively). The temperature of the reaction mixture was maintained at 20  $^{\circ}\text{C}$  by recirculating cold water around the reactor. Seven types of degradation reactions were performed as follows: (i) ultraviolet (UV) radiation (Hg lamp) only (photolysis), (ii)  $\text{H}_2\text{O}_2$  only, (iii) UV radiation +  $\text{H}_2\text{O}_2$ ; (iv) HA NPs only (adsorption); (v)  $\text{H}_2\text{O}_2$  + HA NPs (Fenton-based); (vi) UV radiation + HA NPs (photocatalytic process); and (vii) UV radiation +  $\text{H}_2\text{O}_2$  + HA NPs (photo-Fenton-based process). The volume of  $\text{H}_2\text{O}_2$  (30% v/v) added to the dye solution was 1.33 mL and the mass of HA NPs was 0.13 g (the ratio of the catalyst mass to the oxidizing agent volume was ca. 1:10). For the photocatalytic experiments, a 125 W Hg lamp placed 9 cm away from the solution was used. The total degradation time for all the processes was 2 h.

Degradation experiments were also performed by replacing UV radiation with sunlight and using mirrors to focus natural light inside the reactor. The solar photo-Fenton-based reactions were performed on sunny days at  $35 \pm 5.0$   $^{\circ}\text{C}$  in the laboratories of the Faculty of Exact Sciences and Technology, Federal University of Grande Dourados, Dourados-MS, Brazil ( $22^{\circ}11'41.6''\text{S}$ ,  $54^{\circ}56'00.0''\text{W}$ ). Solar UV radiation (300–400 nm) of ca. 40 W was obtained using a radiometer. The volumes of  $\text{H}_2\text{O}_2$  (30% (v/v)) used for the degradation experiments were 0.66 and 2.00 mL. The mass of the HA NPs was optimized, and 0.066 and 0.2 g of HA NPs were used to identify the optimal degradation conditions in acidic media.

To confirm the discoloration of the reaction mixture (equation 4), a Cary-50 UV-Vis spectrophotometer (Varian, Santa Clara, CA, USA) was used, and the absorbance decay was monitored at 663 nm.

$$\text{Discoloration (\%)} = \left( 1 - \frac{\text{Abs}_{(0)} - \text{Abs}_{(t)}}{\text{Abs}_{(0)}} \right) \times 100 \quad (4)$$

where  $\text{Abs}_{(0)}$  and  $\text{Abs}_{(t)}$  are the initial absorbance and absorbance at time  $t$ , respectively.

TOC measurements were performed using a TOC-VCPN PC-controlled TOC analyzer (Shimadzu, Kyoto, Japan). The measurements were performed at the end of the degradation process to determine the percentage of dye mineralization.

To evaluate the catalytic stability and reusability of the HA NPs, 11 consecutive degradation experiments were performed. At the end of each experiment, the NPs were washed with ultrapure water, recovered using a Nd magnet, and added to a fresh MB dye solution (100 mg L<sup>-1</sup>); the amount of catalyst was not adjusted after each cycle.

The *ortho*-phenanthroline colorimetric method described by the American Public Health Association was used to quantify the residual Fe<sup>2+</sup> ions at the end of the photo-Fenton-based process.<sup>30</sup>

#### Toxicity test of MB dye

*Lactuca sativa* L. seeds were selected, and the smaller and larger seeds were eliminated to standardize their size. Measurements were performed without and with diluting (100, 50, 25, 12.5, and 6.25%) the water generated after MB dye underwent degradation via the photo-Fenton-based reaction. The experiments were performed in triplicate, and Parafilm® paper was used in all the Petri dish containing samples and seeds to avoid seed desiccation. To obtain a control sample, ultrapure water and a 1% zinc sulfate (ZnSO<sub>4</sub>) solution were used as the negative and positive controls, respectively.

During the assay, the samples were placed in a dark environment at a controlled temperature (ca. 25 °C). After incubation, the germinated seeds were counted and the sizes of their roots were measured.

According to Walter *et al.*<sup>31</sup> and Bagur-González *et al.*,<sup>32</sup> to evaluate sample toxicity, the seed development parameters should be calculated, and the collected data can be used to compare the test samples in terms of germination (number of seeds), average root length (cm), percentage of relative seed germination (RSG (%)) (equation 5), relative root growth (RRG (%)) (equation 6), and germination index (GI (%)) (equation 7).

$$\text{RSG (\%)} = \left( \frac{\text{number of germinated seeds per sample}}{\text{number of germinated seeds } \in \text{ negative control}} \right) \quad (5)$$

$$\text{RRG (\%)} = \left( \frac{\text{average length of sample root}}{\text{mean root length } \in \text{ negative control}} \right) \quad (6)$$

$$\text{GI (\%)} = \left( \frac{\text{RSG} \times \text{RRG}}{100} \right) \quad (7)$$

## Results and Discussion

#### Characterization of the modified and unmodified HA NPs

The XRD patterns of all the synthesized HA NPs are shown in Figure 1. The peaks of the (002), (210), (211),

(300), (202), (310), (222), (213), and (004) crystallographic planes of HA (JCPDS No. 09-0432) were observed in the XRD pattern of the unmodified HA NPs.<sup>33</sup>

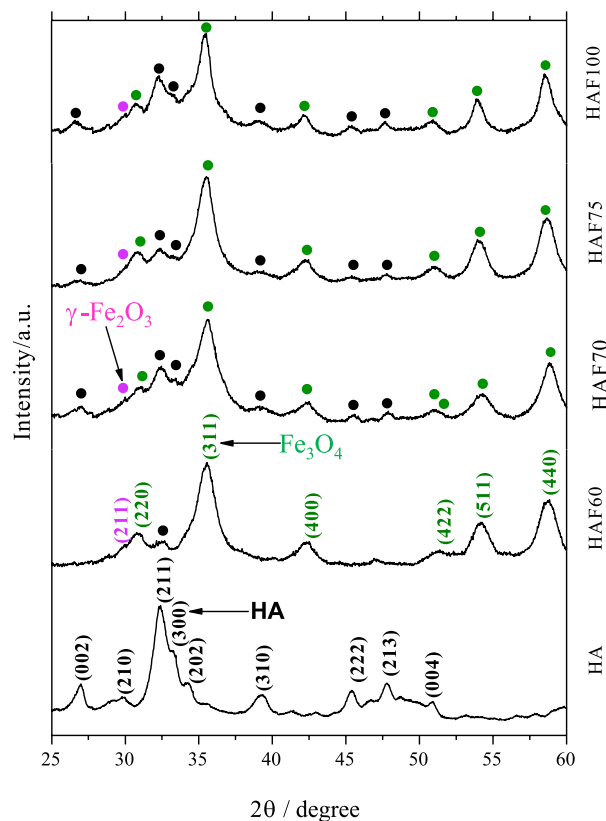


**Figure 1.** X-ray diffraction patterns of unmodified HA NPs and modified HA NPs.

In contrast, the peaks of the (220), (311), (400), (422), (511), and (440) crystallographic planes of γ-Fe<sub>2</sub>O<sub>3</sub> (JCPDS No. 24-0081) and Fe<sub>3</sub>O<sub>4</sub> (JCPDS No. 19-0629) were observed in the XRD patterns of the modified HA NPs. Moreover, the (211) plane, which is characteristic for γ-Fe<sub>2</sub>O<sub>3</sub>, was observed in the XRD patterns of the modified HA NPs. These results demonstrated the presence of a mixed γ-Fe<sub>2</sub>O<sub>3</sub>/Fe<sub>3</sub>O<sub>4</sub> phase in the structure of the modified HA NPs.<sup>34,35</sup>

The characteristic peaks of the unmodified HA NPs were observed in the XDR patterns of all the modified HA NPs, including the HAF100 NP sample, which did not contain Ca<sup>2+</sup> ions. This indicated that the crystallographic structures of the modified and unmodified HA NPs were similar; that is, the Ca<sup>2+</sup> ions in the structure of unmodified HA were replaced by Fe<sup>2+</sup> and Fe<sup>3+</sup> ions.

Therefore, it was concluded that the structure of the HA NPs was modified via Fe<sup>2+</sup>/Fe<sup>3+</sup> doping, and the surfaces of the modified HA NPs were decorated with γ-Fe<sub>2</sub>O<sub>3</sub>/Fe<sub>3</sub>O<sub>4</sub>. These results were in agreement with the findings of Saeki *et al.*<sup>36</sup> who evaluated the introduction

of Fe<sup>2+</sup> and Fe<sup>3+</sup> ions in HA NPs using density functional theory calculations. Moreover, these findings indicated that the Fe<sup>2+</sup> and Fe<sup>3+</sup> ions modified the structure of HA NPs.

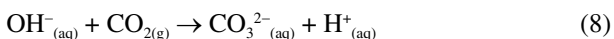
The crystallite sizes of the HAP, HAF60, HAF70, HAF75, and HAF100 samples, which were calculated to be 38.10, 64.87, 32.24, 37.26 and 42.94 nm, respectively, using the Debye-Scherrer equation (equation 3), were within the nanoparticle size range.

The SEM images revealed that the unmodified HA NPs comprised rough, granular, and dense aggregates with a heterogeneous aspect (Figures 2a and 2b). These results were consistent with the findings of Santos *et al.*<sup>37</sup> The SEM images of the HAF60 NPs (Figures 2c and 2d) revealed the presence of spherical  $\gamma$ -Fe<sub>2</sub>O<sub>3</sub>/Fe<sub>3</sub>O<sub>4</sub> particles on the NP surfaces.

The surfaces of the HAF70 (Figures 2e and 2f), HAF75 (Figures 2g and 2h) and HAF100 NPs (Figures 2i and 2j) with higher percentages of Fe<sup>2+</sup>/Fe<sup>3+</sup> ions were smoother, the sizes of the particle agglomerates increased, and particle porosity decreased, indicating that  $\gamma$ -Fe<sub>2</sub>O<sub>3</sub>/Fe<sub>3</sub>O<sub>4</sub> decorated the surfaces of the HA NPs. The HAF100 NPs did not contain Ca<sup>2+</sup> ions in their structure and exhibited a greater degree of modification; that is, their surfaces presented more solid and heterogeneous appearances. Spherical  $\gamma$ -Fe<sub>2</sub>O<sub>3</sub>/Fe<sub>3</sub>O<sub>4</sub> particles were present on the surfaces of all the modified HA NPs, indicating the successful replacement of Ca<sup>2+</sup> ions with Fe<sup>2+</sup>/Fe<sup>3+</sup> ions.

The bands at 569, 603, 873, and 1,047 cm<sup>-1</sup> in the FTIR spectrum of the unmodified HA NPs (Figure 3a), were ascribed to the  $\nu_2$ ,  $\nu_4$ ,  $\nu_1$ , and  $\nu_3$  vibrations, respectively, of the PO<sub>4</sub><sup>3-</sup> groups.<sup>38</sup> Moreover, the peak that emerged at 3,432 cm<sup>-1</sup> was ascribed to the OH<sup>-</sup> groups, and its wide shape indicated that the OH<sup>-</sup> groups vibrated freely. Conversely, the corresponding peaks in the FTIR spectra of the modified HA NPs were narrow, which was ascribed to various fractions of OH<sup>-</sup> ions forming Fe–OH bonds.<sup>39</sup>

The band at 444 cm<sup>-1</sup> in the FTIR spectra of the modified HA NPs was attributed to the Fe–O bonds in the structure of Fe<sub>3</sub>O<sub>4</sub>/ $\gamma$ -Fe<sub>2</sub>O<sub>3</sub>, confirming the modification of the HA NPs. The bands at 1,491, 1,560, and 1,641 cm<sup>-1</sup> represented the molecular vibrations of the CO<sub>3</sub><sup>2-</sup> groups and confirmed the presence of CO<sub>3</sub><sup>2-</sup> groups in the modified NPs; that is, carbonated hydroxyapatite formed spontaneously via the substitution of CO<sub>3</sub><sup>2-</sup> ions in the structure of HA NPs under a non-inert atmosphere (equation 8):<sup>40-42</sup>



As the amount of Ca<sup>2+</sup> ions decreased and the amount of Fe<sup>2+</sup>/Fe<sup>3+</sup> ions increased, the CO<sub>3</sub><sup>2-</sup> groups became increasingly deformed, indicating that the number of OH<sup>-</sup>

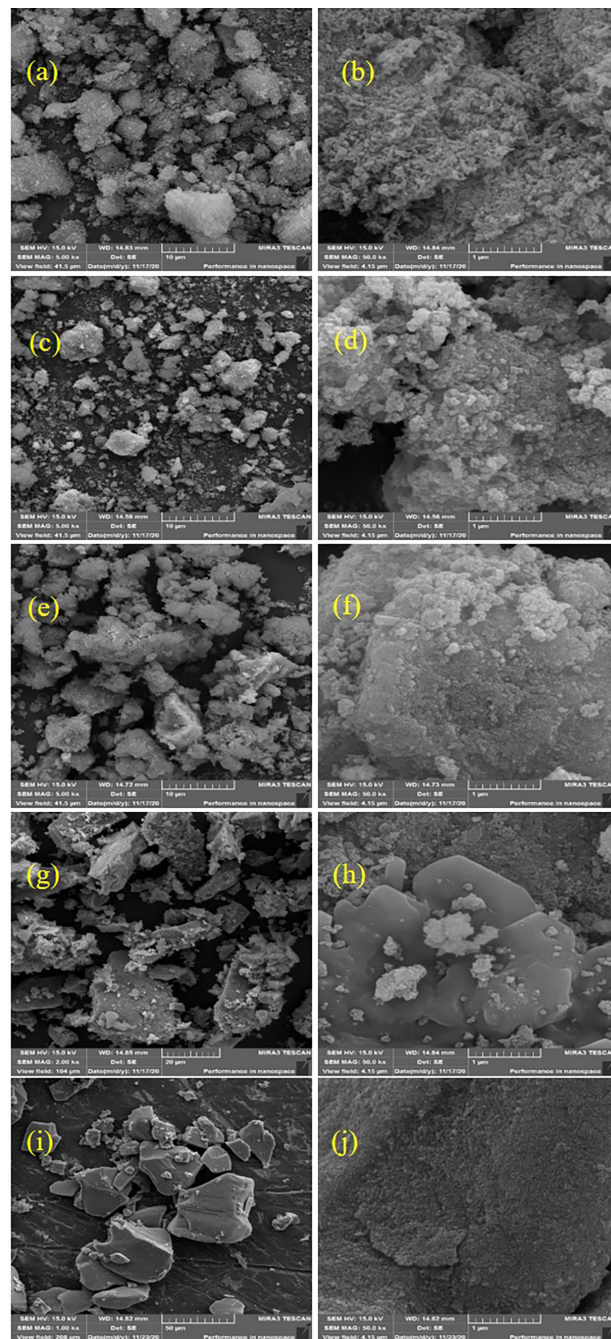


**Figure 2.** SEM-FEG images of (a-b) unmodified HA NPs and modified NPs (c-d) HAF60, (e-f) HAF70, (g-h) HAF75, (i-j) HAF100.

ions that formed Fe–OH bonds increased and the number of OH<sup>-</sup> ions available for carbonation in the presence of CO<sub>2</sub> decreased. This modification was attributed to the ionic radii of Fe<sup>2+</sup>/Fe<sup>3+</sup> being smaller than that of Ca<sup>2+</sup> and strong attraction between the OH<sup>-</sup> ions in the structure and Fe<sup>2+</sup>/Fe<sup>3+</sup> ions.<sup>43</sup>

The Raman spectrum of the HAF75 NPs (Figure 3b) was obtained to complement the FTIR results. The Raman peak at 961 cm<sup>-1</sup>, which was ascribed to the totally symmetric stretching mode ( $\nu_1$ ) of the tetrahedral PO<sub>4</sub><sup>3-</sup> groups (P–O

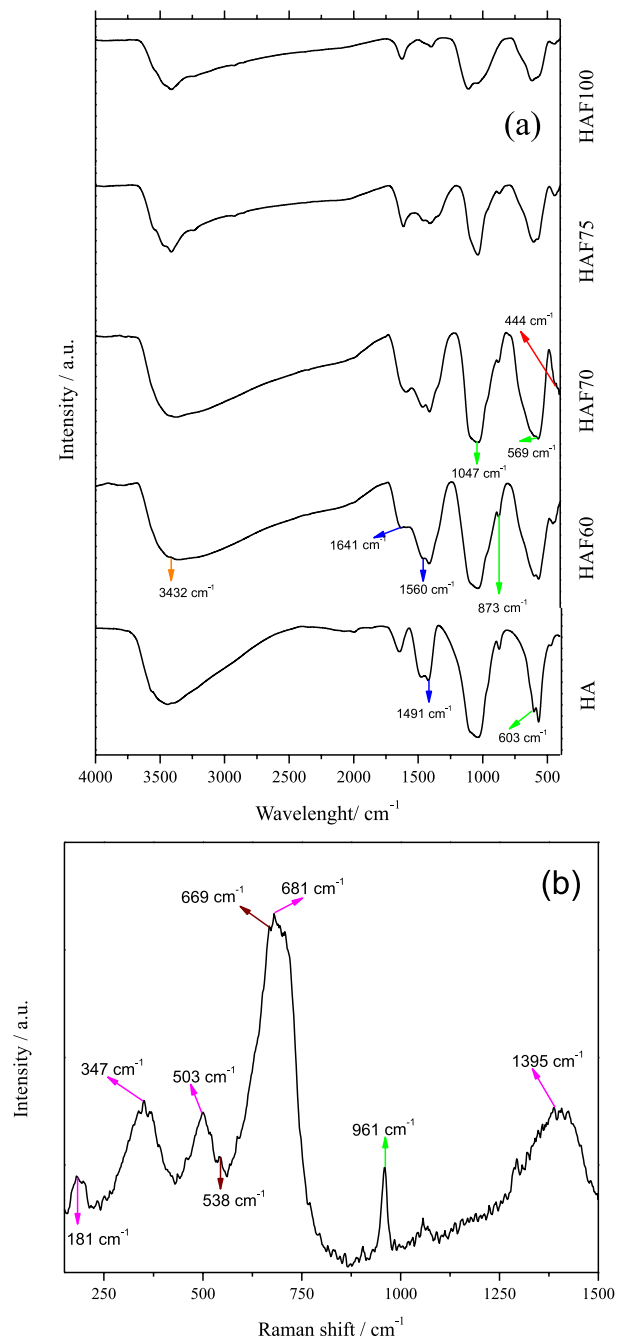


**Figure 3.** (a) FTIR spectrum of the unmodified and modified HA NPs and (b) Raman spectrum of HAF75 NPs.

bonds), was characteristic of HA NPs.<sup>44</sup> Moreover, the presence of Fe<sub>3</sub>O<sub>4</sub> in the structure of the HAF75 NPs was confirmed by its characteristic Raman peaks at 538 and 669 cm<sup>-1</sup>, whereas the presence of γ-Fe<sub>2</sub>O<sub>3</sub> was confirmed by its characteristic Raman peaks at 181, 347, 503, 681, and 1,395 cm<sup>-1</sup>. These data indicated that a mixture of γ-Fe<sub>2</sub>O<sub>3</sub> and Fe<sub>3</sub>O<sub>4</sub> was present in the HAF75 NPs.<sup>45,46</sup>

The HA NPs were thermally decomposed using TG analysis in the temperature range of 25-1000 °C. The TG and differential thermogravimetry (DTG) curves of the HA

NPs are shown in Figure S1a (SI section). The peaks at 100 and 190 °C in the 25-250 °C range of the DTG curves corresponded to the removal of surface and pore water, respectively.<sup>47</sup> In addition, reticular water was lost in the temperatures range of 250-540 °C.<sup>48</sup> The strong endothermic peak in the temperature range of 540-695 °C was attributed to the release of the CO<sub>2</sub> located at the tetrahedral positions of the PO<sub>4</sub><sup>3-</sup> ions in the apatite structure.<sup>49</sup> Decarbonization continued in the temperature range of 700-1000 °C and was accompanied by the dehydroxylation (equation 9) and decomposition of the HA NPs.<sup>50</sup> The decomposition of the HA NPs was a continuous process, which occurred at high temperatures over time.



The residual masses obtained at the end of the thermal decomposition reactions of the HAF75 and HAF70 NPs show a low variation of 86.7 to 90.4%, respectively (Figure S1b, SI section). However, upon analyzing the steps of the thermal decomposition process using DTG, we observed differences in the DTG profiles of the HA NPs. These findings indicated that the amounts of water lost from and CO<sub>2</sub> released by the HA NPs were different, suggesting that the pore sizes and hydration forms of the HA NPs were different. The large residual masses obtained at the end of the experiments indicated that the HA NPs were thermally stable up to 1,000 °C.

Fluorescence measurements were performed to evaluate the effect of the replacement of Ca<sup>2+</sup> ions by Fe<sup>2+</sup>/Fe<sup>3+</sup> ions on all the HA NPs. The obtained spectra are shown in Figure 4.

The maximum peaks at 530.6 nm (green) and 567.2 nm (yellow) were observed in the fluorescence spectra of the unmodified and modified HA NPs, respectively. This

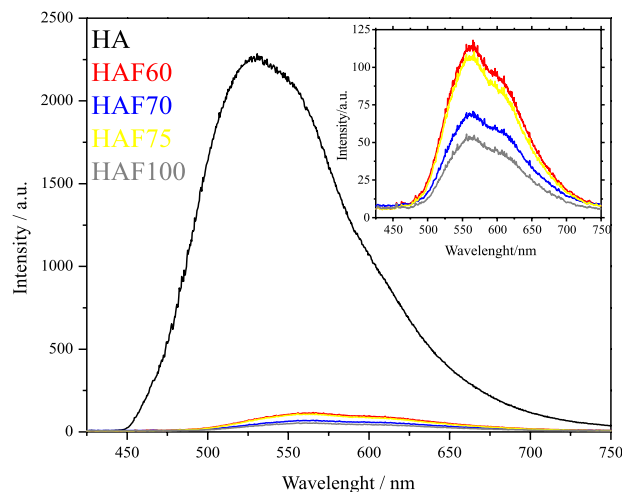


**Figure 4.** Fluorescence spectra of the unmodified and modified HA NPs.

was ascribed to the  $\text{Fe}^{2+}/\text{Fe}^{3+}$  ions attached to the HA NPs re-emitting the light absorbed by the connected electrons. Re-emission required less energy for  $\text{Ca}^{2+}$  fluorescence; therefore, the fluorescence wavelength of the modified HA NPs was higher than that of the unmodified HA NPs.<sup>51</sup>

The fluorescence intensity of the modified HA NPs was significantly lower than that of the unmodified HA NPs because  $\text{Ca}^{2+}$  ions were responsible for the fluorescence of the NPs; therefore, a decrease in the percentage of  $\text{Ca}^{2+}$  ions caused a decrease in material fluorescence.<sup>52,53</sup> Nevertheless, a greater disposition of  $\text{Ca}^{2+}$  ions at the external sites of the crystal structure can occur for some compositions, facilitating the fluorescence response and justifying the changes in the fluorescence order between the HAF70 and HAF75 NPs with similar compositions.

Even though their low-intensity fluorescence signal indicated a low photocatalytic performance, the modified HA NPs exhibited a fluorescence effect, which promoted the degradation process upon irradiation with a wavelength consistent with that of the fluorescence signal.

HA NPs are colloidal particles; therefore, their  $\text{pH}_{\text{PZC}}$  values were determined to evaluate their surface charges. The changes in pH with respect to the initial pH at the 11 points used for all the NPs are presented in Figure 5.

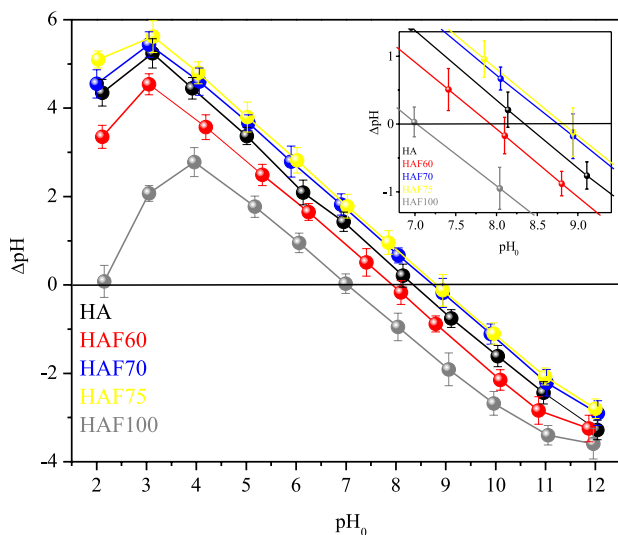


**Figure 5.** Point of zero charge ( $\text{pH}_{\text{PZC}}$ ) of the unmodified and modified HA NPs.

$\text{pH}_{\text{PZC}}$  is defined as the difference between the final pH ( $\text{pH}_f$ ) and initial pH ( $\text{pH}_0$ ) (equation 10). At  $\text{pH}_{\text{PZC}}$  0, the surface of the NPs is neutral, at  $\text{pH}_{\text{PZC}} > 0$ , the surface is negative, and at  $\text{pH}_{\text{PZC}} < 0$  the surface is positive. Therefore, interactions with particles of opposite charges are promoted depending on the  $\text{pH}_{\text{PZC}}$ .<sup>54</sup>

$$\Delta\text{pH} = \text{pH}_f - \text{pH}_0 \quad (10)$$

The  $\text{pH}_{\text{PZC}}$  values of the modified HA NPs were comparable to those of the unmodified HA NPs. However, the  $\text{pH}_{\text{PZC}}$  of the HAF100 NPs, which contained no  $\text{Ca}^{2+}$  ions in their structure, was similar to that of  $\text{Fe}_3\text{O}_4$  (ca. 7.0). This was related to the charges of the ions, for which the attraction strength increased as follows:  $\text{Ca}^{2+} < \text{Fe}^{3+} < \text{Fe}^{2+}$  (according to their charges and sizes).

The  $\text{pH}_{\text{PZC}}$  values of the HA NPs ranged between 7.0 and 8.7. At lower and higher pH values, the surfaces of the NPs presented negative and positive charges, respectively. MB dye, which was used as the target molecule for the degradation experiments, is a cationic dye. The efficiency of the HA NPs for MB dye degradation was evaluated at pH 2.5, 7.0, and 9.0.<sup>55</sup> In other words, the larger the difference in charge between the NP surface and MB dye, the greater the attraction; that is, dye degradation was promoted.

MB dye degradation experiments were not performed at  $\text{pH} > 9.0$  because during MB dye oxidation, abundant iron complexes formed with the  $\text{OH}^-$  ions in the reaction media, which caused the reactive surface area of the NPs to decrease.

#### Photo-Fenton degradation of MB dye

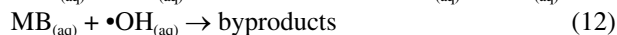
A spectrophotometric study was performed using an MB dye stock solution by monitoring the absorbance of the reaction mixtures. Solutions with different MB dye concentrations ( $5\text{--}100\text{ mg L}^{-1}$ ) were prepared from the stock solution to obtain the calibration curve. The maximum MB dye absorption in aqueous solution was achieved at 663 nm (Figure S2, SI section). The UV-Vis spectra of the MB dye solutions included four absorption bands: two in the visible region (ca. 610 and 663 nm) and two in the UV region (ca. 250 and 300 nm). The band at 663 nm was associated with color removal (chromophore group), and was attributed to bond breaking in relation to the methylene group ( $-\text{RNCH}_3$ ), whereas the bands in the UV region were associated with the  $\pi\text{-}\pi^*$  transitions of the aromatic units.

To analyze the spectral changes ( $\lambda = 663\text{ nm}$ ), equation 3 was used to determine the percentage of discoloration.

Figure 6 shows the discoloration in terms of absorbance decay as a function of time for the MB dye degradation process performed at pH 2.5 (Figure 6a), 7.0 (Figure 6b), and 9.0 (Figure 6c) over the unmodified HA NPs as the catalyst.

For the UV process (photolysis), dye discoloration was significantly higher at pH 9.0 compared with the other pH values, and discoloration reached 53.13%. This was ascribed to the presence of abundant  $\text{OH}^-$  ions in the reaction medium generating a large amount of  $\bullet\text{OH}$  species

through a MB<sup>+</sup> monoelectronic reduction reaction during irradiation, as described by equations 11 and 12.<sup>56,57</sup>



For the degradation reaction using H<sub>2</sub>O<sub>2</sub> as the oxidant, a slight discoloration was observed at all pH values owing to the low effectiveness of H<sub>2</sub>O<sub>2</sub>, which broke the N–C bonds that confer blue color to MB dye. However, upon irradiating the reaction mixtures with UV light, discoloration increased and reached 49.5, 44.6, and 58.1% at pH 2.5, 7.0, and 9.0, respectively. This was attributed to 200–300 nm UV radiation breaking the O–O bonds of H<sub>2</sub>O<sub>2</sub>, as described by equation 13:<sup>58</sup>



For the reaction catalyzed by the unmodified HA NPs in the presence of UV radiation, a discoloration of 38.5% was achieved at pH 2.5. The pH<sub>PZC</sub> measurements revealed that the charge of the HA NPs changed significantly at pH 2.5. The interactions between the NP surface and MB dye, were strong because the pK<sub>a</sub> value of the MB dye molecules was 3.8, and at pH > 3.8 the cationic species were predominant, corroborating the previously reported results.<sup>59</sup> At pH 7.0, the surface charge of the HA NPs did not change significantly, as demonstrated by the pH<sub>PZC</sub> experiments; that is, the attraction of the HA NPs for the MB dye molecules was weak, and a discoloration of only 9.2% was achieved.

For the degradation experiments at pH 9.0, OH<sup>−</sup> ions were slightly attracted to the surface of the HA NPs, as demonstrated by the pH<sub>PZC</sub> data. Conversely, the predominant phase of the MB dye was anionic, promoting its adsorption on the surface of the HA NPs (discoloration of 20.0%). Another possible reaction pathway consisted of the attack of the excess OH<sup>−</sup> ions in the reaction system on MB dye (equations 14 and 15), yielding neutral hydroxy MB (MB–OH) molecules:<sup>60</sup>



The reactions using HA NPs + UV radiation and HA NPs + H<sub>2</sub>O<sub>2</sub> presented low efficiencies. The results of the photocatalytic processes were ascribed to the production of recalcitrant byproducts through a slower reaction pathway during the formation of •OH species. For the HA NPs + H<sub>2</sub>O<sub>2</sub> process, we hypothesized that H<sub>2</sub>O<sub>2</sub> molecules were trapped via interactions with the surface of the NPs; this caused a decrease in the amount of generated

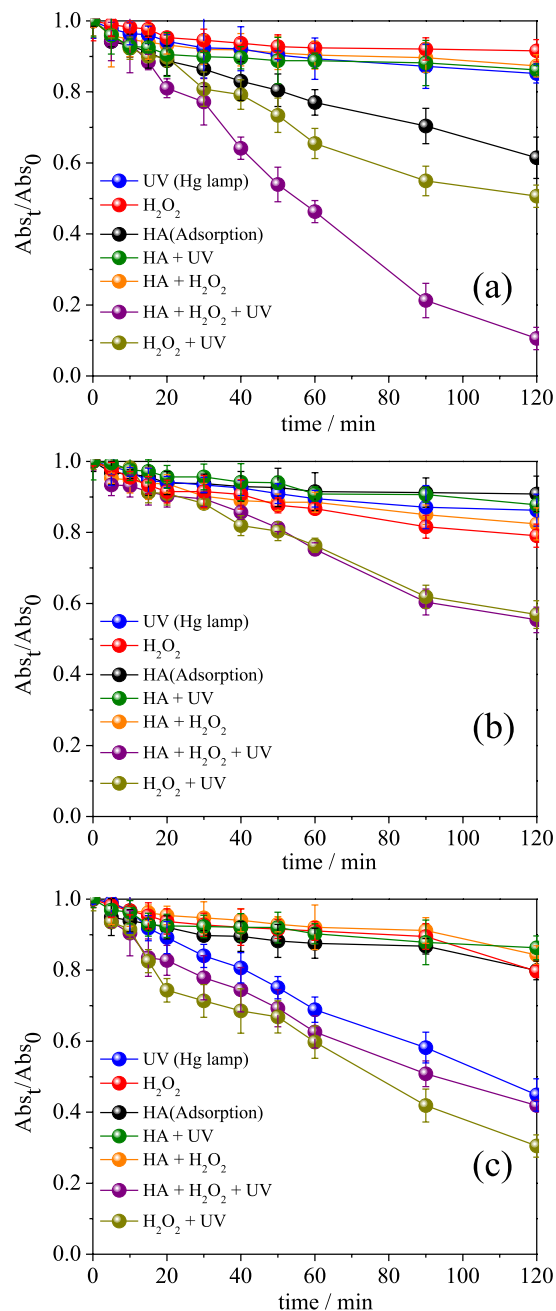
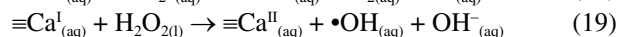
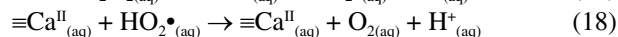
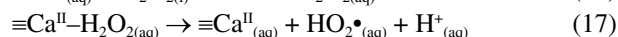
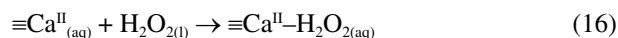


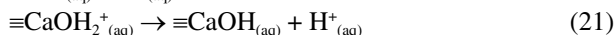
**Figure 6.** Absorbance decay as a function of reaction time for MB dye (100 mg L<sup>−1</sup>) degradation at pH (a) 2.5, (b) 7.0 and (c) 9.0 using 0.13 g of unmodified HA NPs and 1.33 mL of H<sub>2</sub>O<sub>2</sub> (30% v/v).

•OH species and slow reaction kinetics, as indicated by equations 16–19,<sup>61</sup> where ≡ denote surface species:



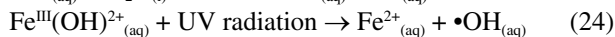
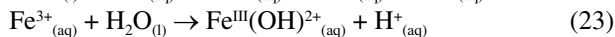
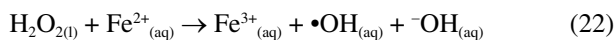
For the HA + H<sub>2</sub>O<sub>2</sub> + UV radiation process, discolorations of 89.4, 44.8, and 58.1% were achieved at pH 2.5, 7.0, and

9.0, respectively. These results further confirmed that the relationship between the  $pK_a$  value of MB dye and pH at the surface of the NPs was a relevant factor for discoloration. At pH 2.5, a strong attraction occurred between cationic MB dye and negative surface of the NPs. By contrast, at pH 9.0, anionic MB dye interacted with the positive surface of the NPs. Both processes promoted surface reactions, which favored discoloration. Therefore, at pH 9.0, the MB dye–HA NP interactions were weak and discoloration was negligible. The amphoteric behavior of the surface of the HA NPs was described by Wu *et al.*<sup>62</sup> and is represented by equations 20 and 21:

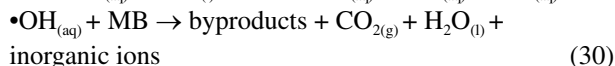
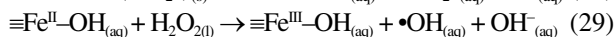
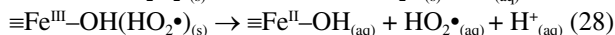
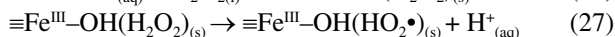
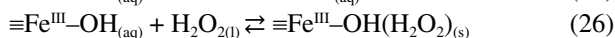


For the degradation process using the modified HA NPs + UV radiation +  $\text{H}_2\text{O}_2$ , which is illustrated in Figure 7, the discoloration values at all pH values were higher than those achieved using unmodified HA NPs + UV radiation +  $\text{H}_2\text{O}_2$ .

This faster reaction kinetics over the modified HA NPs was ascribed to  $\text{Fe}^{2+}/\text{Fe}^{3+}$  ions, which served as the reaction catalyst, accelerating the decomposition of  $\text{H}_2\text{O}_2$  and generating more  $\bullet\text{OH}$  species in the media, as described by equation 22.<sup>63–65</sup> UV light irradiation also induced the reduction of the  $\text{Fe}^{\text{III}}$  aqua complexes in aqueous solution, which generated  $\bullet\text{OH}$  species (equations 23 and 24).<sup>66–68</sup>



The decomposition of  $\text{H}_2\text{O}_2$  by the modified HA NPs was similar to the photo-Fenton-based process, and the oxidation of MB dye was hypothesized to occur according to the reactions described by equations 25–30.<sup>69,70</sup>



The optimal pH for MB dye degradation using modified HA NPs was 2.5 (Figure 7a), and a discoloration of 100% was achieved for all the fabricated HA NPs. These results were consistent with those achieved using the unmodified HA NPs and indicated that the surface load presented a

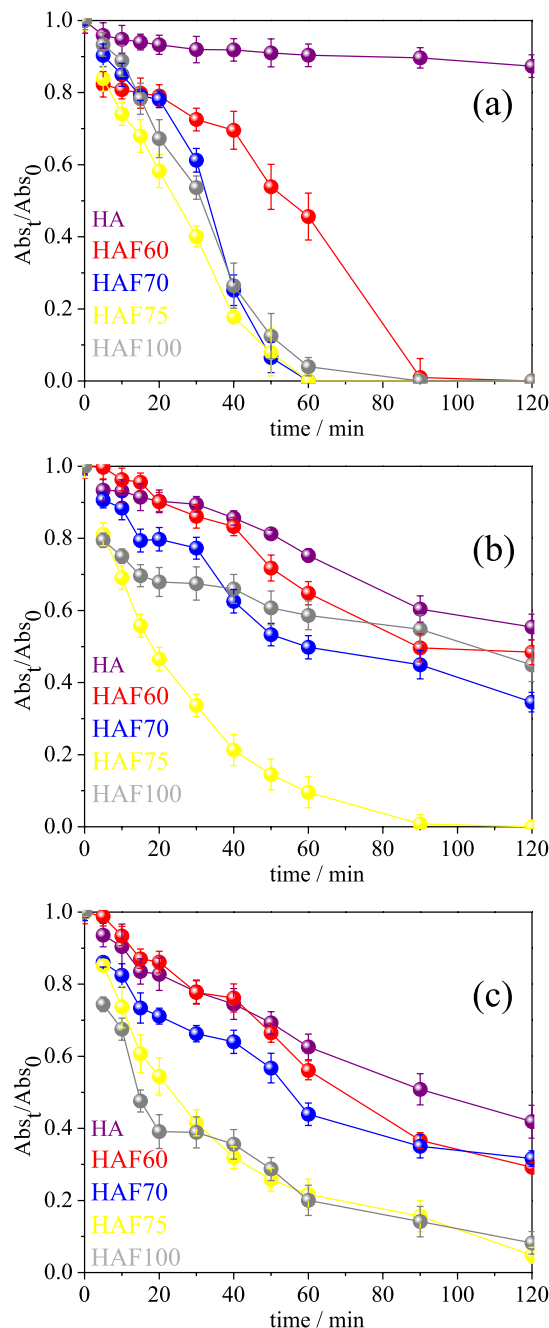
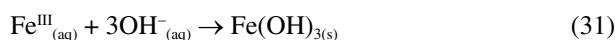


**Figure 7.** Absorbance decay as a function of reaction time for MB dye ( $100 \text{ mg L}^{-1}$ ) degradation at pH (a) 2.5, (b) 7.0 and (c) 9.0 using  $0.13 \text{ g}$  of modified HA NPs and  $1.33 \text{ mL}$  of  $\text{H}_2\text{O}_2$  (30% v/v) by Photo-Fenton-based process.

considerable effect on MB dye discoloration as it facilitated or disrupted the MB dye-catalyst interactions.

At  $\text{pH} > 2.5$ , the abundant  $\text{OH}^-$  ions in the reaction medium passivated the  $\text{Fe}^{2+}/\text{Fe}^{3+}$  ions by forming  $\text{Fe}(\text{OH})_3$  according to the reaction described by equation 31 and interrupted the catalytic cycle, thereby diminishing degradation efficiency.



At pH 7.0, MB dye degradation over the HAF75 NPs achieved a discoloration rate of 100% after 120 min (Figure 7b). Moreover, at pH 9.0, the degradation mechanism was ascribed to the weak attraction between the NP surface and reaction media and weakening of the interactions between the Fe<sup>2+</sup>/Fe<sup>3+</sup> and <sup>-</sup>OH ions by UV radiation, causing the accumulation of •OH species (equations 23 and 24; Figure 7c).<sup>71,72</sup>

Complementary data on MB dye degradation using the modified HA NPs acquired utilizing other analysis methods are presented in Figure S3, and Table S3, SI section, summarizes the data for the degradation of MB dye via photolysis, photocatalysis, Fenton-based, and photo-Fenton-based processes.

The data collected for MB dye degradation at different pH levels using the photo-Fenton-based process prompted us to perform more in-depth analyses utilizing the HAF75 NPs, which yielded the highest discoloration values among all analyzed modified HA NPs.

To determine if the discoloration process coincided with the complete or partial oxidation of the dye, a TOC study was performed for the photo-Fenton-based process using unmodified HA and HAF75 NPs, and the results are presented in Table 1.

**Table 1.** Total organic carbon (TOC) analysis after 120 min of the MB dye degradation by Photo-Fenton-based process

Sample	pH	TOC / (mg L <sup>-1</sup> )	TOC removal / %
MB dye	7.0	59.1	–
A <sup>a</sup>	2.5	36.2	38.7
A <sup>a</sup>	7.0	44.2	25.1
A <sup>a</sup>	9.0	46.6	21.1
B <sup>b</sup>	2.5	6.4	89.1
B <sup>b</sup>	7.0	16.7	71.1
B <sup>b</sup>	9.0	19.6	66.7

<sup>a</sup>Unmodified HA NPs; <sup>b</sup>HAF75 NPs. MB: methylene blue.

At pH 2.5, the mineralization rates of the unmodified HA and HAF75 NPs were high: 38.7 and 89.1%, respectively. This performance was ascribed to the strong attractions between the NP surfaces, reaction media, and MB dye, as indicated by the pH<sub>PZC</sub> of the NPs, which facilitated their interactions.

Upon comparing the efficiencies of the modified and unmodified HA NPs, it was determined that the mineralization effect of the HAF75 NPs was stronger than that of the unmodified HA NPs regardless of the reaction pH. At pH 2.5, the mineralization induced by the HAF75 NPs was 50.4% higher and the degradation time was 60 min shorter than those of the unmodified HA NPs,

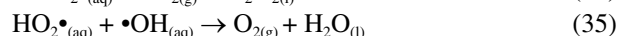
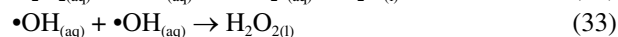
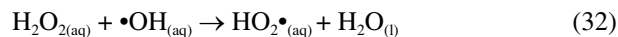
demonstrating that the catalytic activity of the HAF75 NPs was superior to that of the unmodified HA NPs. This was attributed to the modified HA NPs inducing a photo-Fenton-based process for the catalytic reaction unlike the unmodified HA NPs.

Recalcitrant intermediates were formed during the degradation process over the unmodified HA NPs. Moreover, the oxidative strength of the •OH species decreased owing to the large number of parasitic reactions during degradation. Furthermore, the stable Fe<sup>III</sup> complexes formed during the reaction at pH 9.0 over the HAF75 NPs were resistant to oxidation. In addition, the formation of refractory compounds prevented the oxidation of MB dye via •OH species attack.<sup>73</sup>

Makshakova *et al.*<sup>74</sup> achieved a discoloration of 65% during the photocatalytic degradation of MB dye (5 mg L<sup>-1</sup>) over 50 mg of HA NPs doped with Fe<sup>3+</sup> ions under UV irradiation for 2 h. By comparing these results with those obtained for the reaction over the HAF75 NP, it was concluded that the HAF75 NPs induced faster discoloration kinetics, demonstrating the efficiency of the Fe<sub>3</sub>O<sub>4</sub>/γ-Fe<sub>2</sub>O<sub>3</sub> modification.

To optimize the MB dye degradation process, experiments were performed using various catalyst masses, H<sub>2</sub>O<sub>2</sub> (30% (v/v)) volumes, and types of radiation sources. Considering the HAF75 NPs (Figure 8a), the smallest amount of catalyst used for the photo-Fenton-based process promoted the MB dye degradation reaction at pH 2.5, and a discoloration of 100% was reached after 60 min. For these experiments, the volume of H<sub>2</sub>O<sub>2</sub> (30% (v/v)) (2.0 mL) and radiation source (UV) were unchanged. Conversely, the lowest volume of H<sub>2</sub>O<sub>2</sub> (30% (v/v)) (0.66 mL) and lowest mass of catalyst (0.06 g) were the most effective for the degradation of MB dye, favoring the regeneration of Fe<sup>2+</sup> ions during the reaction; therefore, low amounts of Fe<sup>3+</sup> complexes and large amounts of •OH species were formed (Figure 8b).<sup>75,76</sup>

Upon using large volumes of H<sub>2</sub>O<sub>2</sub> and amounts of catalyst, the amount of generated •OH species decreased because the *in situ* formed •OH species directly recombined, thereby slowing reaction kinetics (equations 32-35).<sup>77</sup>



Next, we performed experiments to optimize the type of radiation source (Figure 8c). The discoloration values achieved using the experimental device featuring 15 cm × 15 cm mirror plates (ca. 100% at 60 min) were different from those achieved using UV radiation without

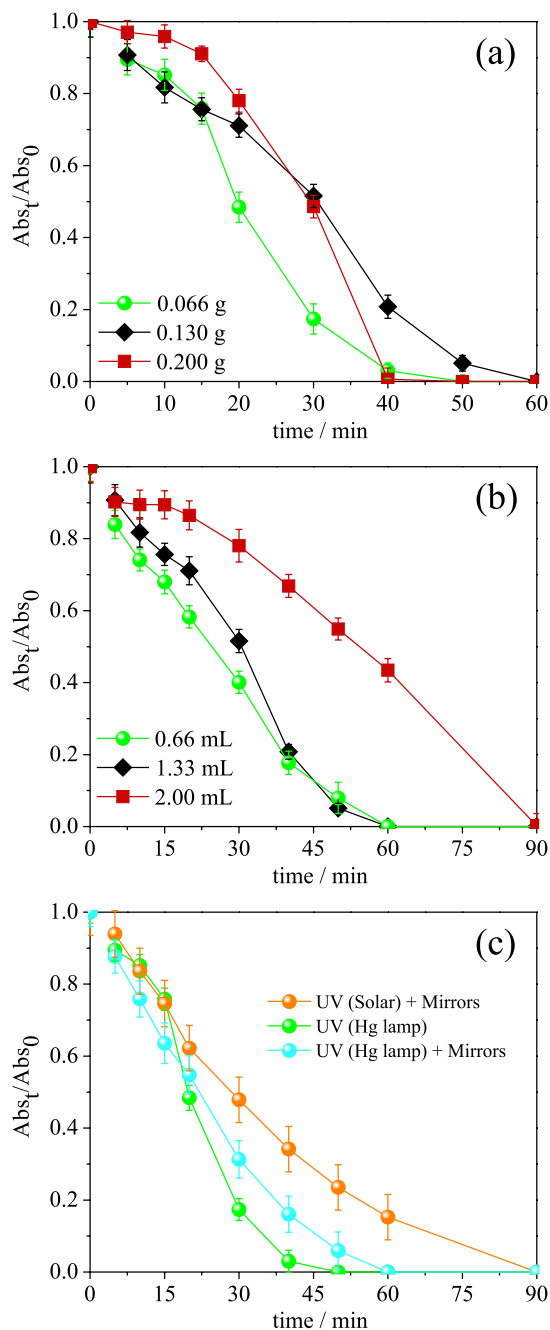


**Figure 8.** Optimization of the parameters of MB dye degradation using HAF75 NPs at pH 2.5: (a) fixed volume of  $H_2O_2$  (30% v/v) (1.33 mL) as a function of catalyst mass, (b) fixed mass of HAF75 NPs (0.06 g) as a function of volume of  $H_2O_2$  (30% v/v) and (c) influence of different radiations sources.

mirrors (ca. 100% at 50 min). Despite the delay in achieving maximum discoloration for the process using solar radiation and mirrors (ca. 100% at 90 min) sunlight is a renewable radiation source that can be used as an alternative to UV radiation for the treatment of dye-contaminated wastewater.<sup>78,79</sup>

For the reactions performed under UV irradiation, there is a high incidence of this source, which caused the

aforementioned radical recombination effects. In contrast, for the reactions performed under sunlight irradiation, mirrors were required to focus the light on the reactor because otherwise degradation occurred slower due to solar radiation dispersion.

#### Reproducibility of catalyst and quantification of residual $Fe^{2+}$ ions

To evaluate catalyst recyclability, MB dye degradation reactions were conducted using the photo-Fenton-based process for 120 min. These reactions were performed under optimized experimental conditions using UV radiation (125 W Hg lamp). At the end of each degradation cycle, the catalyst was separated using a Nd magnet and placed back in the reactor for the next experiment.

The catalyst presented high reproducibility and the average discoloration after 11 consecutive cycles was  $93.5 \pm 4.96\%$  (Figure 9). Furthermore, despite the small loss of catalyst mass during each cycle, the discoloration did not change significantly because once the NP surface was activated by  $H_2O_2$ , it maintained its chemical state and improved discoloration kinetics.<sup>4,20</sup>

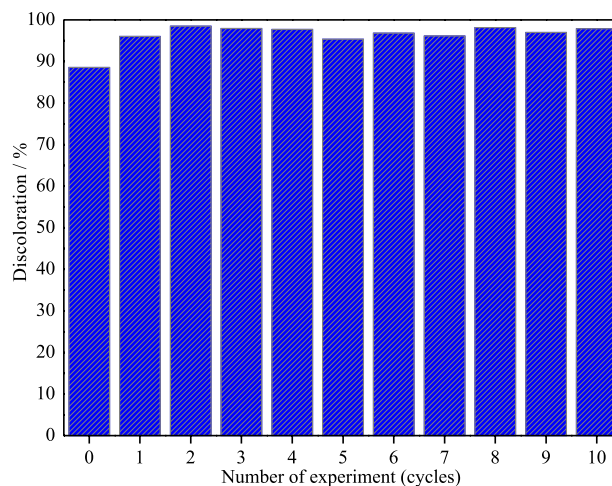
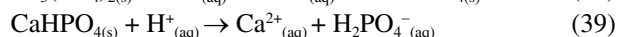
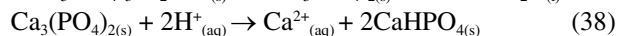
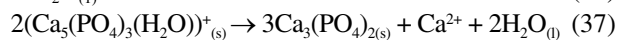
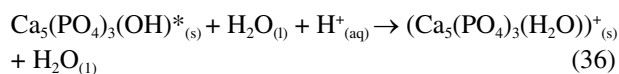


**Figure 9.** Reproducibility test using 0.13 g of HAF75 NPs and 1.33 mL of  $H_2O_2$  (30% v/v) in the MB dye ( $100 \text{ mg L}^{-1}$ ) degradation by Photo-Fenton-based process at pH 2.5.

The *ortho*-phenanthroline method was used to quantify the residual  $Fe^{2+}$  ions (Table S2, SI section) during the MB dye degradation process, and the calibration curve can be described as follows:  $Abs = 0.021 + 0.008[Fe^{2+}]$  (correlation coefficient ( $R^2$ ) = 0.9942) (Figure S4, SI section).  $Fe^{2+}$  concentration was evaluated considering the rules of the CONAMA Resolution (Brazil), which stipulated that the highest admissible concentration of  $Fe^{2+}$  ions in effluents should not exceed  $15 \text{ mg L}^{-1}$ .<sup>80</sup>

The unmodified and modified HA NPs presented

alkaline properties because of the presence of OH<sup>-</sup> ions in their structures. However, at pH 2.5, apatites can be solubilized by reacting with the H<sup>+</sup> ions in the media according to the reactions described by equations 36-39 and, consequently, greater Fe<sup>2+</sup> leaching occurred, as indicated by the data in Table S2.<sup>81</sup>



\*Reduced formula of HA.

Furthermore, upon using the HAF75 NPs for MB dye degradation, the Fe<sup>2+</sup> ion concentration reached 21.6 mg L<sup>-1</sup> at pH 2.5, which exceeded the maximum allowed Fe<sup>2+</sup> ion concentration. Conversely, at pH 9.0, no leached Fe<sup>2+</sup> ions were detected. These results confirmed that at less acidic pH levels, the NPs were more stable and prevented the dissolution of Fe<sup>2+</sup> ions; therefore, the residual Fe<sup>2+</sup> ion concentrations were lower than those stipulated by the rules of the CONAMA Resolution.

The concentration of leached Fe<sup>2+</sup> ions was calculated considering that 0.066 g of HA NPs were used for the degradation of 100 mL of a MB dye solution. However, for the experiment using the HAF75 NPs for 11 consecutive cycles without mass replacement, 1.1 L of MB dye solution (11 cycles involving 100 mL MB dye solution each) were treated using only 0.066 g of HAF75 NPs. Considering the total volume spent and mass of recycled catalyst, the concentration of leached Fe<sup>2+</sup> ions at pH 2.5 was only 1.96 mg L<sup>-1</sup>. Therefore, in heterogeneous degradation systems, there is a small contribution from the homogenous process, leading to a low concentration of dissolved Fe<sup>2+</sup> ions.<sup>7</sup>

#### Post-degradation toxicity of MB dye

*L. sativa* L. seeds were used to evaluate the post-degradation toxicity of MB dye, and the results are listed in Table 2. For the positive control using a 1.0% (m/v) ZnSO<sub>4</sub> solution, seed germination was totally inhibited. Conversely, for the negative control (H<sub>2</sub>O at pH 7.0), 9-10 seeds germinated, and the average root length was 5 cm. These parameters were considered for the other calculations, as presented in Table 2.

Tests were performed using H<sub>2</sub>O at pH 2.5 because the pH of this system was the same as that of the water generated after the MB dye degradation reaction. Nine seeds germinated only after dilution (12.5%), and an RSG

**Table 2.** Seed germination from *Lactuca sativa* L. in the presence of water generated by the MB dye degradation: germination (number of seeds), average root length, percentage relative seed germination (RSG), relative root growth (RRG) and germination index (GI). Experiments were performed in triplicate using 10 seeds

Dilution / %	Sample				
	Positive control ZnSO <sub>4</sub> 1.0% (m/v)	Negative control H <sub>2</sub> O at pH 7.0	H <sub>2</sub> O (pH 2.5)	MB dye / (100 mg L <sup>-1</sup> )	MB dye at pH 2.5 using HAF75
Germination / %					
100	0	9	0	0	0
50	-	-	0	0	0
25	-	-	0	0	7
12.5	-	-	9	0	7
6.25	-	-	9	8	8
Average root length / cm					
100	0	5	0	0	0
50	-	-	0	0	0
25	-	-	0	0	0
12.5	-	-	0	0	1.5
6.25	-	-	1.5	0.4	1.7
Relative seed germination (RSG) / %					
100	0	100	0	0	0
50	-	-	0	0	0
25	-	-	0	0	77.8
12.5	-	-	100	0	77.8
6.25	-	-	100	88.9	88.9
Relative root growth (RRG) / %					
100	0	100	0	0	0
50	-	-	0	0	0
25	-	-	0	0	0
12.5	-	-	0	0	30
6.25	-	-	30.4	8	34
Germination index (GI) / %					
100	0	100	0	0	0
50	-	-	0	0	0
25	-	-	0	0	0
12.5	-	-	0	0	23.3
6.25	-	-	30.4	7.1	30.2

of 100% was achieved, which was equal to that of the negative control. Furthermore, radicles started to form only after 6.25% dilution, and the average size and RRG values of the radicles were 1.5 cm and 30.4%, respectively. The decrease in number of germinated seeds and average root size suggested that acidic media was toxic for the seeds, and as the pH was increased through dilution, the average radicle size and RRG values increased.

The results of the test performed using 100 mg L<sup>-1</sup> of MB dye at pH 2.5 revealed that the reaction medium was highly toxic and germination only occurred after 6.25% dilution (eight germinated seeds, RSG = 88.9%, average root length = 0.4 cm, and RRG = 8%). However, the plants that grew from the seeds presented brown-colored necrotic regions.

Toxicity experiments were performed after the degradation of MB dye at pH 2.5 over HAF75 NPs. At dilutions of 25 and 12.5%, seven seeds germinated and their RSG value reached 77.8%, whereas at a dilution of 6.25%, eight seeds germinated and their RSG value reached 88.9%. A dilution of 25% did not promote root development; however, at a dilution of 12.5%, the root length and RRG value were 1.5 cm and 30%, respectively. At a dilution of 6.25%, the root length and RRG value were 1.7 cm and 34%, respectively, which were slightly higher than those obtained for the seeds tested using H<sub>2</sub>O at pH 2.5.

These results indicated that the toxicity of the MB dye solution obtained after degradation over HAF75 NPs at pH 2.5 was lower than that of a neat MB dye solution. This suggested that the byproducts of the MB dye degradation reaction were less toxic than the original MB solution, thereby confirming the high efficiency of the degradation process.

## Conclusions

Unmodified HA NPs presented remarkable photocatalytic properties. Moreover, HA NPs modified with Fe<sub>3</sub>O<sub>4</sub>/γ-Fe<sub>2</sub>O<sub>3</sub> enhanced the photo-Fenton-based degradation of MB dye. The photo-Fenton-based degradation of MB dye was efficient, and the discoloration rate and TOC removal over unmodified HA NPs at pH 2.5 after 120 min were 88.4 and 38.7%, respectively. In contrast, the discoloration rate and TOC removal over HAF75 NP at pH 2.5 after 60 min were 100 and 89.1%, respectively. These results indicated the remarkable catalytic performance, excellent reproducibility, and outstanding structural stability of the HAF75 NPs, which could be used as catalysts for solar photo-Fenton-based processes. Furthermore, the toxicity test results revealed that the byproducts of the MB dye degradation reaction were less toxic than the MB dye, therefore confirming the effectiveness of the degradation process.

## Supplementary Information

Supplementary data (mass quantity of precursors reagents, quantification of residual iron by *ortho*-phenanthroline method, TG and DTG analysis, UV-Vis spectra of MB

dye, MB dye discoloration for all degradation processes, summary of MB dye discoloration and analytical curve for the quantification of leached Fe<sup>2+</sup> ions) are available free of charge at <http://jbcbs.sbq.org.br> as PDF file.

## Acknowledgments

The authors thank the financial support provided by the Federal University of Grande Dourados (UFGD) and the Brazilian funding agency - Coordenação de Aperfeiçoamento de Pessoal de Nível Superior (CAPES).

## Author Contributions

All authors participated in all stages of the production of article.

## References

1. Hassani, A.; Karaca, M.; Karaca, S.; Khataee, A.; Açışlı, Ö.; Yılmaz, B.; *J. Environ. Manage.* **2018**, *211*, 53. [Crossref]
2. Mohamad, N. D.; Zaki, Z. M.; Amir, A.; *Chem. Eng. J.* **2020**, *393*, 124760. [Crossref]
3. Maruthupandy, M.; Muneeswaran, T.; Anand, M.; Quero, F.; *Int. J. Biol. Macromol.* **2020**, *153*, 736. [Crossref]
4. Costa, G. S.; Althoff, C. A.; Schneider, J. T.; Peralta-Zamora, P.; *J. Braz. Chem. Soc.* **2019**, *30*, 1515. [Crossref]
5. Araujo, F. V. F.; Yokoyama, L.; Teixeira, L. A. C.; Campos, J. C.; *Braz. J. Chem. Eng.* **2011**, *28*, 605. [Crossref]
6. Ike, I. A.; Duke, M.; *J. Contam. Hydrol.* **2018**, *215*, 73. [Crossref]
7. Pinheiro, A. C. N.; Bernardino, T. S.; Junior, F. E. B.; Lanza, M. R. V.; Barros, W. R. P.; *J. Environ. Chem. Eng.* **2020**, *8*, 103621. [Crossref]
8. Silva, V. M.; Gomes Jr., O.; Silva, J. O.; Nossol, A. B. S.; Sousa, R. M. F.; Machado, A. E. H.; Trovó, A. G.; *J. Braz. Chem. Soc.* **2017**, *28*, 1682. [Crossref]
9. Yin, C.; Negreiros, F. R.; Barcaro, G.; Beniya, A.; Sementa, L.; Tyo, E. C.; Bartling, S.; Meiwes-Broer, K. H.; Seifert, S.; Hirata, H.; Isomura, N.; Nigam, S.; Majumder, C.; Watanabe, Y.; Fortunelli, A.; Vajda, S.; *J. Mater. Chem. A* **2017**, *5*, 4923. [Crossref]
10. Oliveira, M. S.; Costa, S. N.; Monteiro, N. K. V.; Neto, P. L.; Magalhães Jr., G. A.; Diógenes, I. C. N.; Araújo, R. S.; Longhinotti, E.; *J. Braz. Chem. Soc.* **2019**, *30*, 2367. [Crossref]
11. Reddy, M. P.; Venugopal, A.; Subrahmanyam, M.; *Appl. Catal., B* **2007**, *69*, 164. [Crossref]
12. Márquez Brazón, E.; Piccirillo, C.; Moreira, I. S.; Castro, P. M. L.; *J. Environ. Manage.* **2016**, *182*, 486. [Crossref]
13. Murgolo, S.; Moreira, I. S.; Piccirillo, C.; Castro, P. M. L.; Ventrella, G.; Coccozza, C.; Mascolo, G.; *Materials (Basel)* **2018**, *11*, 9. [Crossref]

14. Vallet-Regí, M.; Peña, J.; Izquierdo-Barba, I.; *Solid State Ionics* **2004**, *172*, 445. [Crossref]
15. Aparecida, A. H.; Fook, M. V. L.; Santos, M. L.; Guastaldi, A. C.; *Quim. Nova* **2007**, *30*, 892. [Crossref]
16. Shafie, E. R. M.; Ahmad, Z. A.; Ahmad, N.; *Ceram. Int.* **2019**, *45*, 21168. [Crossref]
17. Bakhtiari, L.; Javadpour, J.; Rezaie, H. R.; Erfan, M.; Mazinani, B.; Aminian, A.; *Ceram. Int.* **2016**, *42*, 11259. [Crossref]
18. Arantes, T. M.; Coimbra, L. M. M.; Cristovan, F. H.; Arantes, T. M.; Rosa, G. M.; Lião, L. M.; *J. Braz. Chem. Soc.* **2018**, *29*, 1894. [Crossref]
19. Ma, Q. Y.; Logan, T. J.; Traina, S. J.; *Environ. Sci. Technol.* **1995**, *29*, 1118. [Crossref]
20. Cacciotti, I. In *Handbook of Bioceramics and Biocomposites*; Antoniac, I. V., ed.; Springer: Cham, Switzerland, 2016, ch. 7. [Crossref]
21. Gamal, G. A.; Al-Mufadi, F. A.; Said, A. H.; *Eng. Technol. Appl. Sci. Res.* **2013**, *3*, 532. [Crossref]
22. Deepak, F. L.; Bañobre-López, M.; Carbó-Argibay, E.; Cerqueira, M. F.; Piñeiro-Redondo, Y.; Rivas, J.; Thompson, C. M.; Kamali, S.; Rodríguez-Abreu, C.; Kovnir, K.; Kolenko, Y. V.; *J. Phys. Chem. C* **2015**, *119*, 11947. [Crossref]
23. Vilardi, G.; Bavasso, I.; Scarsella, M.; Verdona, N.; Di Palma, L.; *Process Saf. Environ. Prot.* **2020**, *140*, 46. [Crossref]
24. Behrouzeh, M.; Abbasi, M.; Osfour, S.; Dianat, M. J.; *J. Environ. Chem. Eng.* **2020**, *8*, 103597. [Crossref]
25. Verma, M.; Haritash, A. K.; *J. Environ. Chem. Eng.* **2019**, *7*, 102886. [Crossref]
26. Veisi, H.; Razeghi, S.; Mohammadi, P.; Hemmati, S.; *Mater. Sci. Eng., C* **2019**, *97*, 624. [Crossref]
27. Mahasti, N. N. N.; Shih, Y. J.; Huang, Y. H.; *Sep. Purif. Technol.* **2020**, *247*, 116975. [Crossref]
28. Bento, A. C.; Emídio, E. S.; Hammer, P.; Nogueira, R. F. P.; *J. Braz. Chem. Soc.* **2019**, *30*, 2170. [Crossref]
29. Kosmulski, M.; *Adv. Colloid Interface Sci.* **2020**, *275*, 102064. [Crossref]
30. Krishna Murti, G. S. R.; Moharir, A. V.; Sarma, V. A. K.; *Microchem. J.* **1970**, *15*, 585. [Crossref]
31. Walter, I.; Martínez, F.; Cala, V.; *Environ. Pollut.* **2006**, *139*, 507. [Crossref]
32. Bagur-González, M. G.; Estepa-Molina, C.; Martín-Peinado, F.; Morales-Ruano, S.; *J. Soils Sediments* **2011**, *11*, 281. [Crossref]
33. Shahabi, S.; Najafi, F.; Majdabadi, A.; Hooshmand, T.; Haghbin Nazarpak, M.; Karimi, B.; Fatemi, S. M.; *Sci. World J.* **2014**, *2014*, ID 420616. [Crossref]
34. Rabias, I.; Pratsinis, H.; Drossopoulou, G.; Fardis, M.; Maris, T.; Boukos, N.; Tsotakos, N.; Kletsas, D.; Tsilibary, E.; Papavassiliou, G.; *Biomicrofluidics* **2007**, *1*, 044104. [Crossref]
35. Khan, U. S.; Amanullah; Manan, A.; Khan, N.; Mahmood, A.; Rahim, A.; *Mater. Sci. Pol.* **2015**, *33*, 278. [Crossref]
36. Saeki, S.; Nonami, T.; *Mater. Technol.* **2021**, *36*, 385. [Crossref]
37. Santos, M. H.; de Oliveira, M.; Souza, L. P. F.; Mansur, H. S.; Vasconcelos, W. L.; *Mater. Res.* **2004**, *7*, 625. [Crossref]
38. Timchenko, P. E.; Timchenko, E. V.; Pisareva, E. V.; Yu Vlasov, M.; Red'Kin, N. A.; Frolov, O. O.; *J. Phys.: Conf. Ser.* **2016**, *755*, 012060. [Crossref]
39. Chang, Q.; Xu, W.; Li, N.; Xue, C.; Wang, Y.; Li, Y.; Wang, H.; Yang, J.; Hu, S.; *Appl. Catal., B* **2020**, *263*, 118299. [Crossref]
40. Khalil, M. I.; *Arabian J. Chem.* **2015**, *8*, 279. [Crossref]
41. Iconaru, S. L.; Motelica-Heino, M.; Predoi, D.; *J. Spectrosc.* **2013**, *2013*, ID 284285. [Crossref]
42. Landi, E.; Celotti, G.; Logroscino, G.; Tampieri, A.; *J. Eur. Ceram. Soc.* **2003**, *23*, 2931. [Crossref]
43. Shannon, R. D.; *Acta Crystallogr. Sect. A* **1976**, *32*, 751. [Crossref]
44. Koutsopoulos, S.; *J. Biomed. Mater. Res.* **2002**, *62*, 600. [Crossref]
45. Hanesch, M.; *Geophys. J. Int.* **2009**, *177*, 941. [Crossref]
46. Jacintho, G. V. M.; Corio, P.; Rubim, J. C.; *J. Electroanal. Chem.* **2007**, *603*, 27. [Crossref]
47. Senra, M. R.; de Lima, R. B.; Souza, D. H. S.; Marques, M. F. V.; Monteiro, S. N.; *J. Mater. Res. Technol.* **2020**, *9*, 7190. [Crossref]
48. Sofronia, A. M.; Baies, R.; Anghel, E. M.; Marinescu, C. A.; Tanasescu, S.; *Mater. Sci. Eng., C* **2014**, *43*, 153. [Crossref]
49. Trinkunaite-Felsen, J.; Stankeviciute, Z.; Yang, J. C.; Yang, T. C. K.; Beganskiene, A.; Kareiva, A.; *Ceram. Int.* **2014**, *40*, 12717. [Crossref]
50. Tõnsuaadu, K.; Gross, K. A.; Pluduma, L.; Veiderma, M.; *J. Therm. Anal. Calorim.* **2012**, *110*, 647. [Crossref]
51. Thomas, F.; Serratrice, G.; Béguin, C.; Saint Aman, E.; Pierre, J. L.; Fontecave, M.; Laulhère, J. P.; *J. Biol. Chem.* **1999**, *274*, 13375. [Crossref]
52. Cheng, C.; Tong, K.; Fang, Y.; Wang, J.; Liu, Y.; Tan, J.; *Coatings* **2019**, *9*, 289. [Crossref]
53. Zhang, K.; Zeng, K.; Shen, C.; Tian, S.; Yang, M.; *Microchim. Acta* **2018**, *185*, 225. [Crossref]
54. Khan, M. N.; Sarwar, A.; *Surf. Rev. Lett.* **2007**, *14*, 461. [Crossref]
55. Liu, T.; Li, Y.; Du, Q.; Sun, J.; Jiao, Y.; Yang, G.; Wang, Z.; Xia, Y.; Zhang, W.; Wang, K.; Zhu, H.; Wu, D.; *Colloids Surf., B* **2012**, *90*, 197. [Crossref]
56. Kiwaan, H. A.; Atwee, T. M.; Azab, E. A.; El-Bindary, A. A.; *J. Mol. Struct.* **2020**, *1200*, 127115. [Crossref]
57. Liu, J.; Li, X.; Luo, J.; Duan, C.; Hu, H.; Qian, G.; *Chem. Eng. J.* **2014**, *242*, 187. [Crossref]
58. Kalam, A.; Al-Sehemi, A. G.; Assiri, M.; Du, G.; Ahmad, T.; Ahmad, I.; Pannipara, M.; *Results Phys.* **2018**, *8*, 1046. [Crossref]
59. Sousa, H. R.; Silva, L. S.; Sousa, P. A. A.; Sousa, R. R. M.; Fonseca, M. G.; Osajima, J. A.; Silva-Filho, E. C.; *J. Mater. Res. Technol.* **2019**, *8*, 5432. [Crossref]

60. Mills, A.; Hazafy, D.; Parkinson, J.; Tuttle, T.; Hutchings, M. G.; *Dyes Pigm.* **2011**, *88*, 149. [Crossref]
61. Roumila, Y.; Meziani, D.; Debaghi, S.; Abdmeziem, K.; *Research Square*, **2021**. [Link] accessed in May 2022
62. Wu, L.; Forsling, W.; Schindler, P. W.; *J. Colloid Interface Sci.* **1991**, *147*, 178. [Crossref]
63. Agrawal, S.; Nirwan, N.; Chohadia, A.; *J. Photochem. Photobiol., A* **2020**, *398*, 112547. [Crossref]
64. Ahile, U. J.; Wuana, R. A.; Itodo, A. U.; Sha' Ato, R.; Dantas, R. F.; *Sci. Total Environ.* **2020**, *710*, 134872. [Crossref]
65. Ramalho, M. L. A.; Madeira, V. S.; Brasileiro, I. L. O.; Fernandes, P. C. R.; Barbosa, C. B. M.; Arias, S.; Pacheco, J. G. A.; *J. Photochem. Photobiol., A* **2021**, *404*, 112873. [Crossref]
66. Mitsika, E. E.; Christophoridis, C.; Kouinoglou, N.; Lazaridis, N.; Zacharis, C. K.; Fytianos, K.; *J. Hazard. Mater.* **2021**, *403*, 123819. [Crossref]
67. Lucas, M. S.; Peres, J. A.; *Dyes Pigm.* **2006**, *71*, 236. [Crossref]
68. dos Santosa, V. H. J. M.; Pontin, D.; Oliveira, G. S.; Siqueira, T. A.; Seferin, M.; *Quim. Nova* **2020**, *43*, 599. [Crossref]
69. Hanna, K.; Kone, T.; Medjahdi, G.; *Catal. Commun.* **2008**, *9*, 955. [Crossref]
70. Pignatello, J. J.; Oliveros, E.; MacKay, A.; *Crit. Rev. Environ. Sci. Technol.* **2006**, *36*, 1. [Crossref]
71. Miklos, D. B.; Remy, C.; Jekel, M.; Linden, K. G.; Drewes, J. E.; Hübner, U.; *Water Res.* **2018**, *139*, 118. [Crossref]
72. Stroparo, E. C.; Mollinari, K. C.; de Souza, K. V.; *Polimeros* **2018**, *28*, 400. [Crossref]
73. Medrano-rodríguez, F.; Picos-benítez, A.; Brillas, E.; Bandala, E. R.; *J. Electroanal. Chem.* **2020**, *873*, 114360. [Crossref]
74. Makshakova, O. N.; Shurtakova, D. V.; Vakhin, A. V.; Grishin, O.; Gafurov, M. R.; *Crystals* **2021**, *11*, 1219. [Crossref]
75. Verma, V.; Chaudhari, P. K.; *Arabian J. Chem.* **2020**, *13*, 5084. [Crossref]
76. Audino, F.; Companyà, G.; Pérez-Moya, M.; Espuña, A.; Graells, M.; *Sci. Total Environ.* **2019**, *646*, 902. [Crossref]
77. Fast, S. A.; Gude, V. G.; Truax, D. D.; Martin, J.; Magbanua, B. S.; *Environ. Process.* **2017**, *4*, 283. [Crossref]
78. Ortega-Liévana, M. C.; Sánchez-López, E.; Hidalgo-Carrillo, J.; Marinas, A.; Marinas, J. M.; Urbano, F. J.; *Appl. Catal., B* **2012**, *127*, 316. [Crossref]
79. Arzate, S.; Campos-Mañas, M. C.; Miralles-Cuevas, S.; Agüera, A.; García Sánchez, J. L.; Sánchez Pérez, J. A.; *J. Environ. Manage.* **2020**, *261*, 110265. [Crossref]
80. Conselho Nacional do Meio Ambiente (CONAMA); Resolução No. 430, de 13 de maio de 2011, Dispõe sobre As *Condições e Padrões de Lançamento de Efluentes, Complementa e Altera a Resolução No. 357, de 17 de março de 2005, do Conselho Nacional do Meio Ambiente*; Diário Oficial da União (DOU), Brasília, No. 92, de 16/05/2011, p. 89. [Link] accessed in May 2022
81. Dorozhkin, S. V.; *World J. Methodol.* **2012**, *2*, 1. [Crossref]

Submitted: January 26, 2022

Published online: May 27, 2022

